

# Visualization of surfactant-enhanced nonaqueous phase liquid mobilization and solubilization in a two-dimensional micromodel

Lirong Zhong<sup>1</sup> and Alex Mayer<sup>2</sup>

Department of Geological Engineering and Sciences, Michigan Technological University, Houghton, Michigan

Robert J. Glass

Flow Visualization and Processes Laboratory, Sandia National Laboratories, Albuquerque, New Mexico

**Abstract.** Surfactant-enhanced aquifer remediation is an emerging technology for aquifers contaminated with nonaqueous phase liquids (NAPLs). A two-dimensional micromodel and image capture system were applied to observe microscale NAPL mobilization and solubilization phenomena. In each experiment a common residual NAPL field was established, followed by a series of mobilization and solubilization experiments. Mobilization floods included pure water floods with variable flow rates and surfactant floods with variations in surfactant formulations. At relatively low capillary numbers ( $N_{ca} < 10^{-3}$ ) the surfactant mobilization floods resulted in higher NAPL saturations than for similar  $N_{ca}$  pure water floods. These differences in macroscopic saturations are explained by differences in microscale mobilization processes. Solubilization of the residual NAPL remaining after the mobilization stage was dominated by the formation of microscale dissolution fingers, which produced nonequilibrium macroscale NAPL solubilization. A macroemulsion phase also was observed to form spontaneously and persist during the solubilization stage of the experiments.

## 1. Introduction

Nonaqueous phase liquids (NAPLs) and their component chemicals have become pervasive subsurface groundwater contaminants. Once released into the subsurface, NAPLs migrate downward through the vadose zone toward the water table. Denser-than-water NAPLs, or DNAPLs, penetrate the water table and continue to move downward into the aquifer, displacing the resident water. Once the bulk volume of the DNAPL release has been exhausted, water reinvades a portion of the aquifer, fragmenting the DNAPL into a series of high-saturation pools separated by regions of lower saturation where DNAPL is trapped as residual in discrete ganglia, or blobs, within the pore space.

Conventional DNAPL remediation efforts, such as pump-and-treat, involve increasing the groundwater gradient through the DNAPL-contaminated area. However, impractically large gradients are needed to mobilize trapped DNAPLs. Under typical conditions the viscous forces imposed by the aqueous phase gradient are not large enough to overcome the high capillary forces that trap the DNAPL in place. These capillary forces are due to the high interfacial tension (IFT) between the DNAPL and aqueous phases. Furthermore, because of the relatively low aqueous solubilities of DNAPLs, large quantities

of groundwater are required to completely dissolve the trapped DNAPLs. To address these problems, surfactant-enhanced removal of NAPLs is emerging as an aquifer remediation technology that shows promise in increasing the efficiency of DNAPL remediation. Surfactant solutions work to mobilize trapped NAPLs by lowering the interfacial tension. The addition of surfactants above the critical micelle concentration also enhances the solubilization of entrapped NAPLs in the aqueous phase, by incorporating NAPL components into surfactant micelles.

The macroscale processes affecting DNAPL migration and remediation include immiscible displacement of water by DNAPLs (and vice versa), trapping of DNAPL as pools or residual, mobilization of trapped DNAPL, and DNAPL dissolution or solubilization. Each of these macroscale processes is controlled by underlying microscale physics, where we define the microscale as ranging from the single pore to several hundreds or thousands of pores. Most modeling efforts that predict DNAPL migration and dissolution or design systems for remediating DNAPLs are based on macroscale approaches. However, an understanding of the microscale is critical for assessing the accuracy of macroscale predictions, especially for evaluating innovative remediation technologies. For example, consider the macroscale nonequilibrium solubilization observed in column experiments by Mayer *et al.* [1999] for an anionic surfactant-NAPL system. They hypothesized that the observed nonequilibrium behavior is due either to rate limitations in chemical reactions, mass transfer resistance at the NAPL-aqueous interface, or physical phenomena such as bypassing or dissolution fingering, all of which act at the microscale. Determining which microscale mechanism is responsible for the observed macroscale behavior is critical for proper

<sup>1</sup>Now at Center for Petroleum and Geosystems Engineering, University of Texas, Austin, Texas.

<sup>2</sup>On sabbatical at Department of Hydrology and Ecology, Delft University of Technology, Delft, Netherlands.

formulation of macroscale models of the solubilization process.

Several experimental methods have been developed to study NAPL distribution, mobilization, and dissolution at the microscale. Solidification methods rely on introducing NAPLs into the porous media to establish a residual saturation, followed by in situ solidification of NAPL blobs and separation from the porous media [e.g., *Conrad et al.*, 1992; *Mayer and Miller*, 1992]. Transparent cells filled with a monolayer of glass beads have been used to visualize NAPL distributions at the pore scale [e.g., *Mayer and Miller*, 1993]. Glass cells etched with idealized pore networks also have been used for NAPL visualization [e.g., *Conrad et al.*, 1992] and to consider mass transfer rates for NAPL dissolution in fresh water [*Jia et al.*, 1999]. In the petroleum industry, such visualization techniques also have been employed to investigate pore-scale, multiphase flow phenomena [e.g., *Egbogah and Dawe*, 1980; *Hornbrook et al.*, 1991], including a study involving surfactants [*Mahers et al.*, 1981] that considered the influence of aqueous phase flow rates on displacement behavior and blob size and shape distributions. A shortcoming of all these visualization studies has been their qualitative nature.

Recently, methods based on two-dimensional (2-D), full-field, quantitative energy transmission techniques [e.g., *Tidwell and Glass*, 1994] have been developed and applied to increase our understanding of single- and two-phase flow and transport processes at both the macroscale and microscale. These methods have been applied to thin but extensive, heterogeneous sand slabs, where saturation is integrated over the thickness of the slab [e.g., *Glass and Nicholl*, 1996; *Glass et al.*, 2000]. Additionally, these methods have been applied to 2-D transparent micromodel pore networks or fractures, where not only can the phase occupancy be quantitatively monitored in time but also the pore geometry at the time of the experiment can be measured with great accuracy and precision. Combining the geometry and phase occupancy allows the detailed quantitative study of a wide range of microscale phenomena such as gravity-driven fingering [*Nicholl et al.*, 1993], phase entrapment [*Nicholl and Glass*, 1994], and entrapped phase dissolution [*Glass and Nicholl*, 1995]. In the present work, we apply quantitative light transmission techniques to study the microscale behavior of surfactant-enhanced NAPL mobilization and solubilization in a transparent micromodel.

## 2. Experimental Design

We designed experiments to make use of high-resolution, quantitative visualization techniques based on light transmission to measure micromodel pore geometry, phase structure, and phase saturation as a function of time. In each experiment the water-saturated micromodel was first invaded with NAPL until the phase structure, composed of flowing NAPL and entrapped water, was stable in time. Following this simulated NAPL release, injection was switched to water, thus mobilizing and entrapping NAPL at a residual saturation within the flowing water phase. This residual NAPL structure formed the common starting point for subsequent remediation experiments where surfactant-enhanced NAPL mobilization and solubilization were studied. We designed the mobilization experiments to systematically vary the dimensionless capillary number  $N_{ca}$  via the interfacial tension between the NAPL and the injected aqueous surfactant solution. The capillary number, which relates viscous forces to capillary forces, can be used

to quantify the potential for mobilization. The capillary number can be defined as

$$N_{ca} = \frac{q\mu}{\sigma \cos \theta}, \quad (1)$$

where  $q$  is the Darcy velocity of the displacing fluid,  $\mu$  is the dynamic viscosity of the displacing fluid,  $\sigma$  is the IFT between aqueous phase and NAPL, and  $\theta$  is the contact angle of the aqueous phase to the solid material (assumed to be zero for all systems). The IFT was varied by changing the chemistry of the surfactant solution. Another series of mobilization experiments was conducted with pure water floods, where  $N_{ca}$  was varied by changing the injection rate of the water. The surfactant and water flood mobilizations were followed with a surfactant flood to consider the influence of surfactant chemistry and initial NAPL saturation on surfactant-enhanced solubilization. Changes in the chemistry of the surfactant solution also produced variations in NAPL solubility.

### 2.1. Experimental System

The experimental system consisted of a transparent micromodel, associated plumbing, and a quantitative light transmission measurement system (see Figure 1a). The micromodel was formed by two pieces of roughened glass plate (15 cm × 30 cm) held together with an external fluid pressure of 138 kPa (see Figure 1b). This configuration is directly analogous to a rough-walled fracture, for which similar models have been used extensively in single- and two-phase flow process studies [e.g., *Nicholl and Glass*, 1994; *Glass and Nicholl*, 1995; *Nicholl et al.*, 1999; *Detwiler et al.*, 2000]. However, the micromodel also forms an analog to a 2-D granular porous medium where the contact points and regions of very small aperture between the two glass plates correspond to the contact points between the grains. The grain contact points, roughly 2–4 correlation lengths apart, are separated by larger gap regions that likewise correspond to the pores within the granular media. In many ways this micromodel may be more representative of coarse-grained aquifer material than the typical etched and fused plates used by others [e.g., *Conrad et al.*, 1992; *Jia et al.*, 1999].

The micromodel was oriented horizontally, and its long sides were sealed with a Viton gasket. At the inflow end of the micromodel a manifold was installed along the open aperture to distribute fluids evenly. Fluid was delivered to the micromodel from reservoirs weighed continuously on scales to monitor inflow rates. Four syringe needles were installed at the outflow end of the fracture, each connected to one of four independent syringes held in a syringe pump. The syringe pump was used to pull fluids through the micromodel. This design allowed even outflow from four points at the micromodel edge by eliminating mobilized NAPL blob plugging. Traps were built in each of the four effluent tubing assemblies to capture mobilized NAPL. When mobilized NAPL mixed with aqueous phase passed through the traps, the denser NAPL sank to the bottom and remained in the traps while aqueous phase was withdrawn by the syringe pump. The NAPL level in the traps was monitored and recorded by a video camera. Digital images collected from the video camera were analyzed to determine the cumulative NAPL volume mobilized from the micromodel.

The quantitative light transmission measurement system was composed of a feedback-controlled, constant output light table and high-resolution (2048 × 2048 pixels, 4096 gray level), liq-

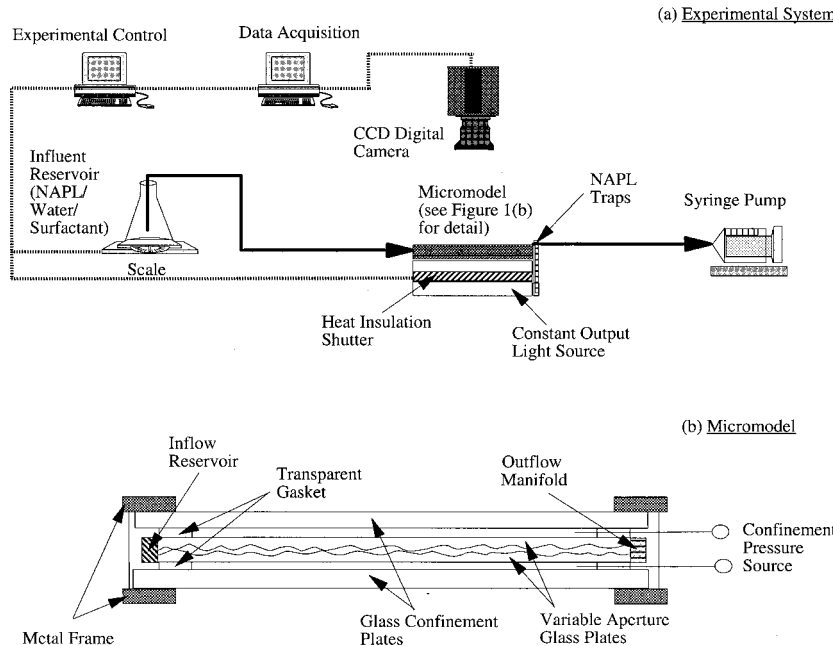


**Figure 1.** Schematic illustration of the (a) experimental system and (b) micromodel.

uid-cooled and shuttered, CCD digital camera (Photometrics). Additional details of this system are given by *Detwiler et al.* [1999]. Each pixel of the CCD measured a 0.15 mm by 0.15 mm region of the micromodel. Images of the micromodel were captured at an exposure time of 0.30 s with intervals ranging from 15 s to 1 hour. Because the NAPL-surfactant solution interactions, such as IFT and solubility, are temperature sensitive, a motorized heat-insulating shutter was installed between the micromodel and the light box. All data acquisition and storage procedures were automated, as was most of the experimental system control such as image collection and insulated shutter movement. Conventional cameras and a video recorder also were utilized to collect qualitative, visual information as each experiment progressed.

## 2.2. Fluid Solutions and Properties

The surfactant solution contained 1.6% by weight sodium dihexyl sulfosuccinate (Aerosol MA-80I, CYTEC Chemicals, West Paterson, New Jersey) as the surfactant and 4% by weight isopropanol (IPA) as a cosolvent (Aldrich Chemical Company, Milwaukee, Wisconsin). Sodium dihexyl sulfosuccinate is an anionic surfactant with two hydrophobic tails. The surfactant solution also contained various concentrations of NaCl (reagent grade, Aldrich Chemical Company): 0.18%, 0.30%, and 0.60% by weight. The aqueous solubilities and the NAPL-aqueous interfacial tensions vary with electrolyte concentration for anionic surfactants such as sodium dihexyl sulfosuccinate. The NAPL used in this study was trichloroethylene (TCE) (>99.5% pure, Aldrich Chemical Company) dyed with Oil-red-O (Aldrich Chemical Company) at concentration of 0.5 g/L.

Interfacial tensions between TCE and surfactant solutions were measured using a spinning drop tensiometer (Kruss USA, Charlotte, North Carolina). TCE and surfactant solutions were preequilibrated before being injected into the spinning capillary. During all measurements the temperature of the spinning capillary was controlled at  $23.5^\circ \pm 0.2^\circ\text{C}$  using an oil bath. The

measured values of IFT between TCE and surfactant solutions and the solubility of TCE in these solutions measured from batch experiments are listed in Table 1. At least 13 sets of IFT measurements were made for each of the surfactant solutions. Literature values were used for the pure water-TCE IFT and solubility [*Mercer and Cohen*, 1990]. As expected, as the salt concentration increases, the IFT decreases, and the solubility of TCE increases. The solubilities are from 4 to 10 times the solubility in pure water. Viscosities of the surfactant solutions were measured with either a Brookfield DV-II viscometer fitted with a small-sample adapter (Brookfield Engineering Laboratories, Stoughton, Massachusetts) or a Contraves LS-30 Couette viscometer (Contraves, Inc., Bern, Switzerland).

## 2.3. Experimental Sequence

The experimental sequence for all experiments consisted of four stages: a TCE flood, a water flood, a mobilization flood, and a solubilization flood. The flow was directed along the long axis of the micromodel. The temperature of the micromodel was held at  $23.5^\circ \pm 0.5^\circ\text{C}$ . The sequence began by saturating the micromodel with water, followed by TCE flooding at a flow rate of 0.20 mL/min. The TCE flood continued until no more

**Table 1.** Solution Properties

Composition <sup>a</sup>	Interfacial Tension, <sup>b</sup> dyn/cm	Dynamic Viscosity, cP	Solubility, ppm
Surf., 0.18%	$0.95 \pm 0.12$	1.25	3920
Surf., 0.30%	$0.62 \pm 0.08$	1.63	5080
Surf., 0.60%	$0.23 \pm 0.01$	1.80	9950
Pure water	34.5 <sup>c</sup>	1.09	1100 <sup>c</sup>

<sup>a</sup>Surf., surfactant solution, where percentages indicate NaCl concentration by weight, 1.6% MA-80I surfactant by weight, and 4.0% IPA by weight.

<sup>b</sup>Mean plus or minus standard deviation.

<sup>c</sup>*Mercer and Cohen* [1990].

**Table 2.** Summary of Experiments

Experiment <sup>a</sup>	Water Flood ( $v = 0.0022$ cm/s)				Mobilization Stage				Solubilization Stage ( $v = 0.020$ cm/s): Composition
	TCE Flood ( $v = 0.0022$ cm/s <sup>b</sup> ): $S_n^c$ After Flood, %	$S_n$ After Flood, %	Blob Length <sup>d</sup> After Flood, mm	$v$ , cm/s	Number of Pore Volumes in Flood	Flood Composition <sup>e</sup>	Flood Capillary Number	$S_n$ After Flood, %	
	After Flood, %	After Flood, %	After Flood, mm	cm/s	in Flood	Flood Composition	Capillary Number	Flood, %	
1	55.3	42.6	1.73 ± 3.05	0.020	1.7	surf., 0.18%	2.9E-4 <sup>f</sup>	35.0	surf., 0.18%
7	60.1	42.3	1.66 ± 2.61	0.020	1.7	surf., 0.18%	2.9E-4	37.1	surf., 0.18%
2	58.1	43.1	1.83 ± 2.51	0.020	1.7	surf., 0.30%	4.2E-4	27.6	NA <sup>g</sup>
3	57.7	43.0	1.76 ± 2.58	0.020	1.7	surf., 0.30%	4.2E-4	30.9	NA
6	57.0	40.6	1.88 ± 2.61	0.020	1.7	surf., 0.30%	4.2E-4	35.5	surf., 0.30%
15	57.5	37.7	1.49 ± 2.39	0.020	1.7	surf., 0.30%	4.2E-4	29.4	surf., 0.30%
16	61.9	42.0	1.48 ± 2.65	0.414	5.6	surf., 0.30%	7.9E-3	0.4	surf., 0.30%
4	60.0	39.1	1.52 ± 2.33	0.020	1.7	surf., 0.60%	1.2E-3	15.4	surf., 0.60%
5	65.7	46.9	1.92 ± 2.68	0.020	3.8	surf., 0.60%	1.2E-3	9.6	surf., 0.60%
8	59.9	46.2	1.62 ± 2.48	0.020	6.4	surf., 0.60%	1.2E-3	16.9	surf., 0.60%
9	59.3	45.9	1.50 ± 2.50	0.112	3.8	pure water	4.0E-5	36.5	surf., 0.30%
14	56.6	36.9	NM <sup>h</sup>	0.112	3.8	pure water	4.0E-5	28.5	surf., 0.30%
10	60.1	38.9	1.56 ± 2.48	0.550	6.4	pure water	2.0E-4	22.3	surf., 0.30%
11	57.8	38.4	1.41 ± 2.44	2.75	32.1	pure water	1.0E-3	14.6	surf., 0.30%
12	59.5	43.6	1.30 ± 2.51	2.75	32.0	pure water	1.0E-3	15.2	surf., 0.30%
13	62.2	42.9	1.54 ± 2.53	2.75	31.0	pure water	1.0E-3	18.6	surf., 0.30%
17	57.7	37.8	1.33 ± 2.34	5.50	7.0	pure water	2.0E-3	14.0	surf., 0.30%
Mean	59.2	40.1	1.60						
Standard deviation	2.5	3.1							

<sup>a</sup>Experiment number corresponds to chronological order of experiments.

<sup>b</sup>Here,  $v$ , saturated pore velocity, equal to  $Q/(dw)$ , where  $Q$  is the volumetric flow rate,  $d$  is the mean aperture size, and  $w$  is the micromodel width.

<sup>c</sup> $S_n$ , NAPL saturation.

<sup>d</sup>Geometric mean plus or minus geometric standard deviation (log millimeters).

<sup>e</sup>Surf., surfactant solution, where percentages indicate NaCl concentration by weight, 1.6% MA-80I surfactant by weight, and 4.0% IPA by weight.

<sup>f</sup>Read 2.9E-4 as  $2.9 \times 10^{-4}$ .

<sup>g</sup>NA, solubilization stage not performed for this experiment.

<sup>h</sup>NM, not measured.

water was displaced from the micromodel. Water was then reintroduced to the micromodel at a flow rate of 0.20 mL/min, entrapping the TCE at an initial residual saturation. The water flood continued until TCE was no longer displaced. This sequence produced the common initial point for all of the mobilization-solubilization experiments.

The entrapped NAPL was then mobilized by flushing either with pure water or aqueous surfactant solutions, at a range of velocities and IFTs. Displacement of NAPL blobs occurs when the viscous forces exerted by the invading wetting (aqueous) phase exceed the capillary forces holding them in place. Capillary desaturation curves typically are used to characterize the mobilization of residual fluids at the macroscale from porous media subjected to viscous floods [Lake, 1989]. These curves relate the remaining residual saturation to the value of  $N_{ca}$  estimated for the displacing fluid.

A total of 17 mobilization and solubilization experiments were conducted. Table 2 shows the fluids, average fluid pore velocities (defined as the volumetric flow rate divided by the mean aperture size and micromodel width), and corresponding capillary numbers during each stage of the experiments. The mobilization stage continued until no TCE was observed to flow. The number of pore volumes (defined as the full aperture volume of the micromodel) of injected mobilization fluid is indicated for each experiment in Table 2. The surfactant solution was not preequilibrated with the NAPL prior to the invasion of the micromodel, but minimal solubilization of NAPL occurred during the mobilization stage.

When the mobilization was completed, the solubilization stage began and continued until all or most of the remaining residual TCE was solubilized. In the experiments where surfactant floods were used in the mobilization stage (10 experiments, see Table 2) the same surfactant solution was used in the solubilization stage, and the two stages were continuous. Where pure water was used in the mobilization stage (seven experiments, see Table 2), the micromodel influent was switched from the pure water reservoir to the surfactant solution reservoir at the beginning of the solubilization stage. The range of surfactant formulations used in the solubilization stage (see Table 2) produced a range of TCE solubilities. Some experiments were repeated: Experiments 1 and 7; experiments 6 and 15; experiments 4, 5, and 8; experiments 9 and 14; and experiments 11, 12, and 13 were replicates.

The mobilization stages lasted from several minutes to an hour, while solubilization stages lasted from several hours to 4 days. Effluent aqueous samples were collected for two of the experiments during the solubilization stage (experiments 12 and 13). During periods of effluent sampling, an infusion pump was used to deliver liquid to the micromodel through the inflow manifold. Effluent liquids were directed into vials pre-filled with a known amount of water to minimize TCE volatilization and to dilute the effluent samples. An SRI 8610C gas chromatograph (SRI International, Menlo Park, California) with a flame ionization detector was used to determine TCE concentrations.

The micromodel was monitored by digital imaging, video,

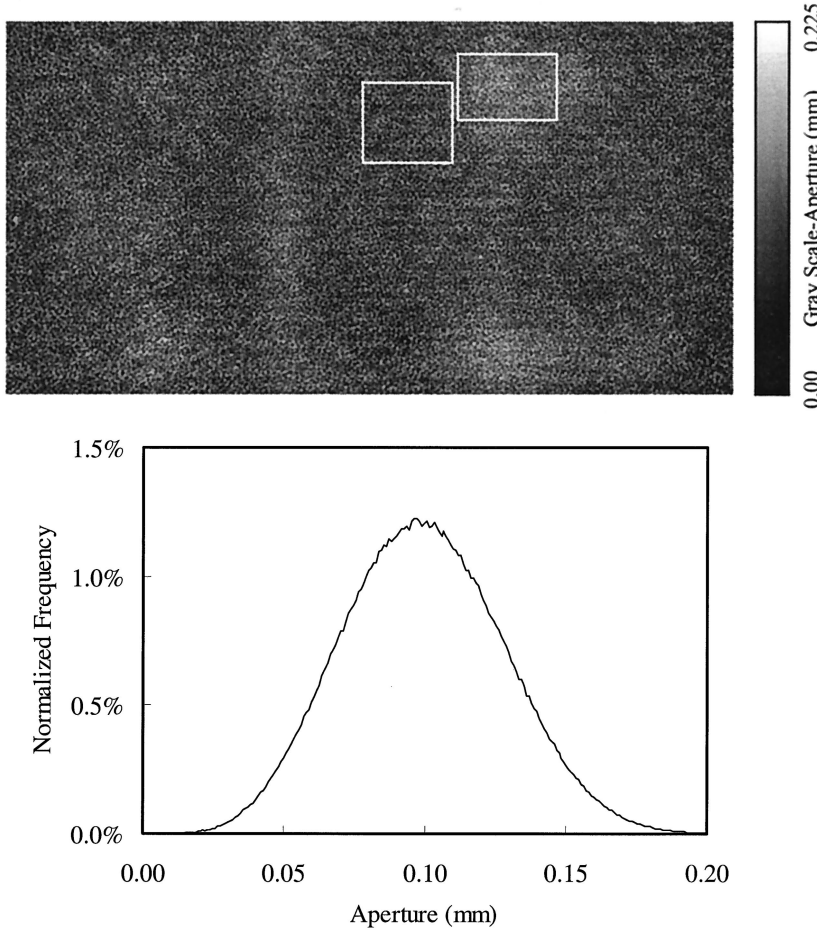


**Figure 2.** Image of the aperture field and frequency distribution of aperture sizes. The gray scale in the image indicates the aperture size. The left and right rectangular regions near the top of the micromodel show where concentrated areas of large and small apertures, respectively, occur in the field.

and conventional camera systems during the complete course of a test. The digital image data were processed as described in section 2.5 to provide total NAPL saturations and discrete NAPL blob geometry data. Effluent NAPL volume in the traps was recorded from the beginning of test till the end of the mobilization flood. After each experiment, sulfuric acid (18 M) with 38 g/L Nochromix was flushed through the micromodel to remove surfactant, residual NAPL, and residual dye. Clean water was then pumped through the micromodel until the effluent pH reached 6.

#### 2.4. Measurement of Micromodel Aperture Field and Volume

The micromodel aperture field was measured using light transmission and the protocol of *Detwiler et al.* [1999]. In this protocol the aperture field normalized by the mean of the aperture field is first measured at a series of dye concentrations. Precision- and accuracy-based error are then assessed to determine the dye concentration that yields the minimum error. The mean aperture is then measured independently and applied to obtain the dimensional aperture field. Using water dyed with FD&C blue #1 (Warner-Jenkinson, St. Louis, Missouri), the minimum error field was found for a dye concentration of 0.06 g/L, yielding a root-mean-square error of 1.1% of the mean aperture. To obtain the dimensional aperture field, a known volume of water was injected into the initially

dry micromodel such that about three fourths of the micromodel was filled. The area occupied by water was measured by image analysis using the binarization algorithms described in section 2.5. The volume divided by area gives the mean aperture in the region occupied by the fluid. Combining the normalized aperture field for the same water-occupied region with this mean aperture yields the dimensional aperture field. Averaging the dimensional aperture field over the entire field yields the mean aperture (0.0998 mm) and the micromodel pore volume ( $4.68 \text{ cm}^3$ ). Differences in the measurements of the mean aperture before and after all of the experiments were within the measurement error ( $\sim 0.3\%$ ), demonstrating that the micromodel structure did not change significantly over the course of the experiments.

Figure 2 is an image of the aperture field and the aperture distribution. The aperture distribution follows a normal distribution with values ranging up to 0.225 mm and a standard deviation of 0.028 mm. Spatial correlation lengths were determined from the aperture field using Geostatistical Software Library (GSLIB) [Deutsch and Journel, 1998] as 0.70 mm and 0.82 mm in the short-axis and long-axis directions, respectively. In Figure 2 we also clearly see large-scale heterogeneity within the field that is not captured by the geostatistical analysis. These larger-scale heterogeneities, of the scale of about one third of the micromodel width ( $\sim 5 \text{ cm}$ ), superimpose a slight

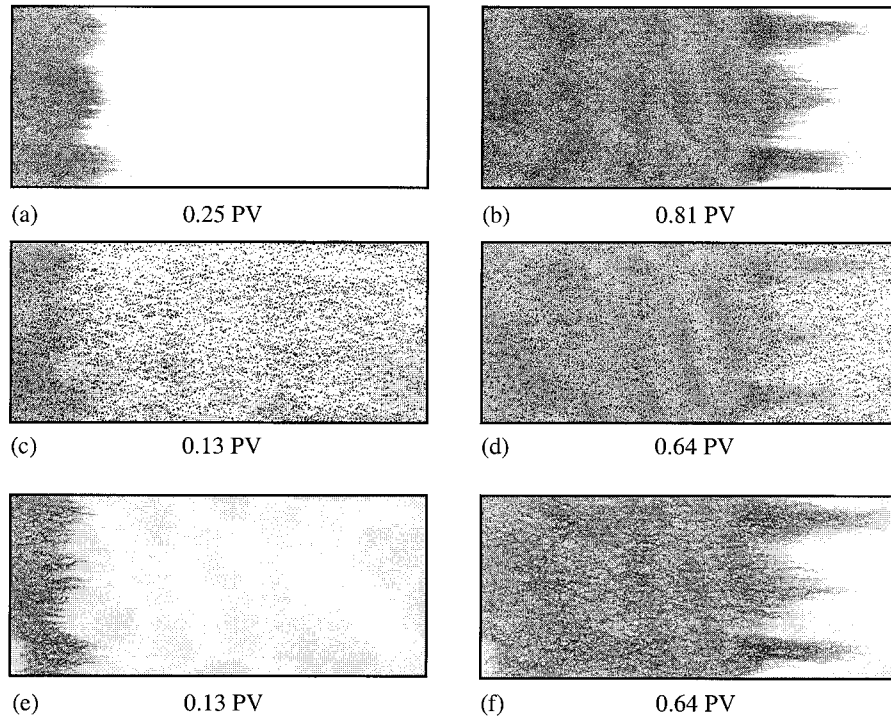


**Figure 3.** Visualization of the flow field. Images show the flow pattern at different pore volumes (PV) of dye solution flushed: (a and b) images from a dye test without trapped NAPL, (c and d) images from a dye test with trapped NAPL, and (e and f) images where the trapped NAPL has been subtracted from the images in Figures 3c and 3d, respectively. Direction of flow is left to right in images. Dye is gray in the image, and dark blobs in Figures 3c and 3d indicate trapped NAPL.

undulating structure on top of the smaller-scale random field. For example, consider the two regions designated in Figure 2. One region represents an area with larger apertures (predominately white), and the other region represents an area with smaller apertures (predominately black). The region with larger apertures has a mean aperture size that is 23% greater than the full-field mean, while the mean aperture size in the region with smaller apertures is 5% lower than the full-field mean.

To demonstrate the influence of the aperture field heterogeneity on the fluid flow, a dye solution was pumped through the micromodel at a pore velocity of 0.022 cm/s. Shown in Figure 3 are images of the dye solution flush at two different times with and without NAPL at a residual saturation of 12%, which is a typical saturation at the end of the mobilization stage of the experiments. Figures 3a–3f show the two scales of variability in the flow characteristics. The larger-scale variability (on the order of centimeters) is demonstrated by the three dye “fingers” that are ahead of the average position of the dye front. The smaller-scale variability (on the order of millimeters) is demonstrated by the finer fingers distributed around the larger-scale variability. In addition, a comparison of Figures 3a and 3b with Figures 3e and 3f shows that the residual NAPL has a negligible influence on the large-scale flow pattern at this low saturation. However, at the higher saturations typical of the end of the water flood stage, the occurrence of residual NAPL is very important in defining the aqueous flow structure, as has been demonstrated previously by *Nicholl and Glass [1994]*.

## 2.5. Experimental Image Processing and Measurement of NAPL Saturation and Blob Geometry

The image-processing scheme is shown in Figure 4. The first step is to adjust the gray levels in each image to compensate for slight temporal fluctuations in light source intensity. A light transmitting wedge with a range of constant density steps was installed next to the micromodel and included in each experimental image in order to monitor the intensity of the source. Small fluctuations in transmitted light intensity are removed by

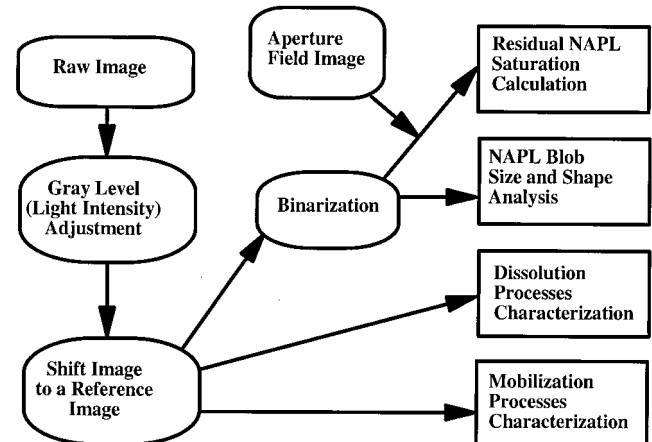


**Figure 4.** Schematic illustration of image-processing procedure.

adjusting intensities of experimental images to those in a reference image. After gray level adjustment, images were corrected for slight shifts caused by occasional vibrations of the test stand to a tolerance of 0.05 of a pixel. Further details on gray level adjustment and shifting are given by *Detwiler et al.* [1999].

The differences in transmitted light intensity between NAPL and aqueous phases were used to transform raw images to binary phase distribution images where each pixel occupied by either NAPL or aqueous phase is represented by a 1 or 0, respectively. The light transmitted through the micromodel varies over the entire field, especially near the cell edges. Thus a single threshold intensity value cannot be used to binarize the entire field. Instead, we use the adaptive thresholding technique, where a local histogram is employed to define a local threshold for binarization [Nicholl and Glass, 1994]. The percent distance between the local peaks for NAPL and water is chosen for a given field to best match the binarized and raw images by eye. An approximately 0.5 cm swath along the edges of the micromodel was excluded from the binarized field, and thus the saturation estimates, because the transparent gasket for the confinement gas chamber disturbed the light transmission at its inner edge. The excluded area was 9.8% of the total micromodel area.

The product of the binarized phase structure and the aperture field, summed over the image, yields the NAPL volume within the image. Dividing this volume by the total image volume yields the NAPL saturation  $S_n$ . The binarized images of trapped NAPL were also used for blob size and shape measurement. The blob area, perimeter, and length were measured using Clemex Vision software (Clemex Technologies, Canada). The blob length was defined as the direction of the largest span of a blob in the average flow direction (the long dimension of the micromodel).

The accuracy of binarization impacts both the total phase saturation and NAPL blob geometry measurements. In order to evaluate the possible error in these measurements we chose the distance between the NAPL and water peaks in the binarization algorithm to be slightly higher and lower than that found to give the best binarization by eye. Each of these distances were chosen to yield a small but noticeable overestimate and underestimate of the area occupied by the NAPL, yielding a deviation in total saturation of 3% and in the mean blob length of 2%. These differences are considered to represent the possible maximum error of the image-based measurements. To further assess the accuracy of NAPL saturation measurement by image processing, the total saturations obtained through image processing were compared with those based on a total volume balance using inflow and outflow trap data. The average, absolute difference between the mean  $S_n$  based on image processing and the mean  $S_n$  based on volume balance after the TCE flood is 0.6% and after the water flood is 1.9%, both well within measurement error.

### 3. Results and Discussion

In sections 3.1–3.3, we describe the results for each of the experimental stages. The NAPL distributions after the water flood are described in section 3.1. This stage provided the common initial condition for the mobilization experiments, which are described in section 3.2. The NAPL saturations and distributions after mobilization by the pure water and surfactant floods are analyzed and compared. Finally, the fluid phase

behavior during the solubilization stage of the experiments is described in section 3.3.

#### 3.1. NAPL Distribution Prior to Mobilization and Solubilization Stages

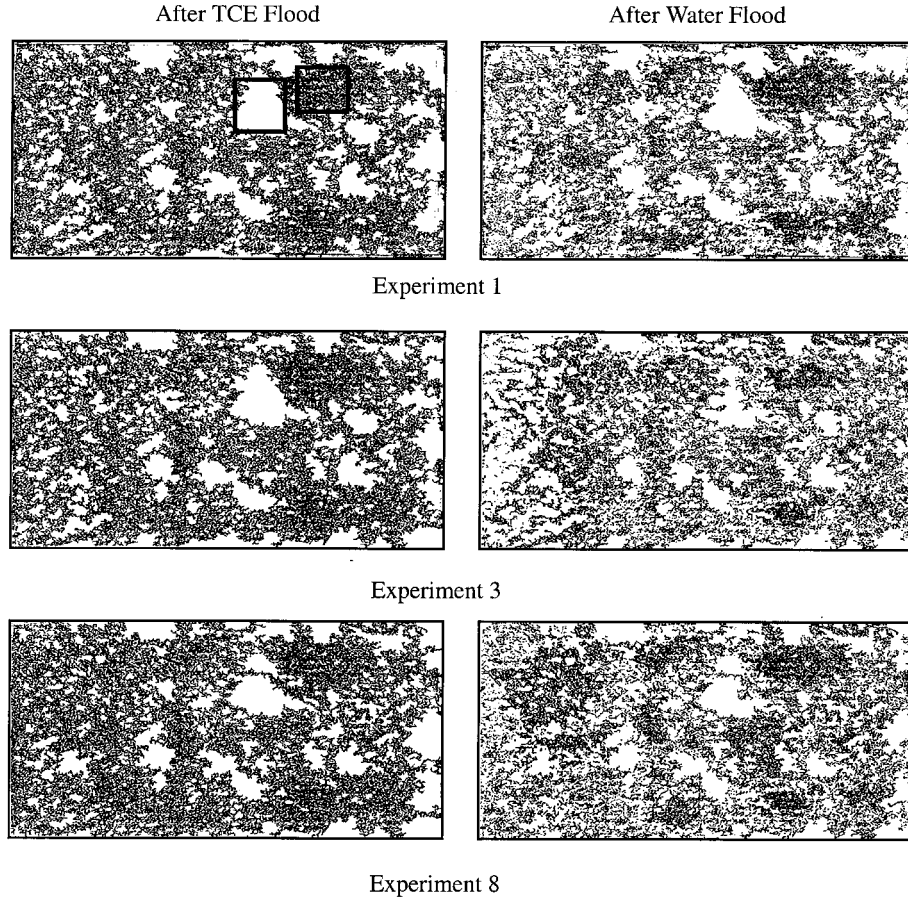
TCE saturations in the micromodel after TCE floods and water floods are listed in Table 2. The mean TCE saturation was  $59.2 \pm 2.5\%$  and was  $41.6 \pm 3.1\%$  after the TCE floods and the water floods, respectively. The outlier TCE saturation (experiment 5) was caused by an aberrantly high flow rate at the beginning of the TCE flood. Example NAPL structures after the TCE and water floods from three experiments are shown in Figure 5. These images show that the complex NAPL structure is controlled not only by small-scale heterogeneities in the aperture field but also by heterogeneities at the larger scale identified earlier in the aperture field measurements and dye displacement experiments (see Figures 2 and 3). NAPL is consistently found at higher saturations in regions of larger average mean aperture, both after the TCE flood and after the water flood, yielding a base phase structure that is similar from experiment to experiment. However, we also see that while the structures following each of the floods are similar and the saturations are nearly the same, no two structures are ever identical.

Table 2 lists the geometric mean and standard deviation of blob length in the direction of average flow (the long side of the micromodel) for each experiment, following the water flood and prior to the mobilization stage. The pooled arithmetic mean among the geometric means also is given in Table 2. The results in Table 2 indicate that there is significant variability among the blob size distributions prior to the mobilization stage. Furthermore, there is a trend toward smaller blob sizes in time across the experimental set (i.e., as the experiment number increases). This trend could be caused by a change in the effective contact angle as the micromodel aged during the course of the experiments. Changes in the effective contact angle can be caused by roughening of the glass surface due to etching by the acid solutions used to clean the glass or, alternatively, by the contamination of the glass surface by residual materials over time. However, comparison of replicate experiments for both water and surfactant floods shows no apparent correlation between the initial conditions, as characterized by NAPL saturations and/or blob size statistics, and the saturations and/or blob size statistics following mobilization.

#### 3.2. Mobilization of Residual NAPL

Phase structures midway through mobilization floods for water and a range of surfactant solutions are shown in Figure 6. For the water flood (Figure 6a), NAPL movement occurs simultaneously over the entire aperture field and forms a series of long “rivulets” oriented in the direction of flow. Alternatively, in surfactant floods a visible front of high NAPL saturation forms (Figures 6b–6d) that sweeps the entire width of the cell. The images in Figures 6b–6d suggest that as the IFT between the surfactant solution and NAPL decreases, the tendency to form a concentrated front increases.

Close inspection of the evolving phase structure during water floods shows that blobs first stretch in the downstream direction and combine with other stretching blobs to form long rivulets. At the trailing edge of a rivulet we find snapping off and shedding of entrapped blobs at a smaller size than in the initial field. Rivulets often travel through previously NAPL-free areas, especially when capillary numbers for water mobi-



**Figure 5.** Comparison of NAPL distributions following TCE floods and water floods for three experiments. The left and right rectangular regions in the upper left image show concentrated areas of apertures empty or filled with NAPL, respectively, occur in the field. The rectangular regions correspond approximately with rectangular regions in Figure 2. Black pixels indicate areas where NAPL is present. White pixels indicate areas where aqueous phase is present. Direction of flow is left to right in images.

lization are large. Simultaneous rivulet formation throughout the field prevents the formation of a front. The extension of blobs in the direction of flow also was observed by *Wardlaw and McKellar* [1985] in a column packed with glass beads, where larger blobs fissioned repeatedly upon mobilization, resulting in the reentrainment of the smaller daughter blobs. In our case, the extension of blobs was greater and more frequent than that observed by *Wardlaw and McKellar* [1985], resulting in larger numbers of reentrapped, smaller daughter blobs.

Inspection of the phase structure during surfactant floods shows that as the surfactant moves into the residual NAPL field, mobilization is restricted to a narrow zone, whereas the NAPL downstream of the front is completely undisturbed. As this zone moves further into the field, mobilized NAPL congregates to form a high-saturation NAPL front. Behind the mobilization front the NAPL field is composed of small blobs that are nearly uniformly distributed within the micromodel. Formation of a NAPL front has been observed by others in the petroleum engineering literature [e.g., *Larson and Hirasaki*, 1978; *Larson*, 1979; *Pope*, 1980], where it has been conceptually correlated to downstream mobilization. While downstream mobilization indeed contributes to the formation of the front, close inspection of the developing phase structure in our experiments shows that at the leading edge of the front, NAPL also migrates upstream against the mean direction of flow.

Figure 7 shows a sequence of images from experiment 8; the arrows indicate the migration of a portion of a blob occurring in the countercurrent direction. This upstream migration is caused by a capillary force imbalance within the blob, due to an up to 2 orders of magnitude difference in IFTs between the upstream and downstream edges of the blob.

Images of trapped NAPL after mobilization are presented in Figure 8 for a range of capillary numbers. All images show the same region within the micromodel. We see in Figure 8 that for both water floods (images in Figures 8a, 8b, 8c, and 8f) and surfactant floods (images in Figures 8d, 8e, 8g, and 8h) the trapped TCE blobs become smaller and less complicated as  $N_{ca}$  increases. The maximum blob length and the geometric mean blob length are given in Figure 9 as a function of  $N_{ca}$ . Both the maximum and geometric mean blob length display an approximately inverse relationship with  $N_{ca}$  with overlap between the water and surfactant floods. This inverse relationship is suggested by simple force balances as presented by *Mayer and Miller* [1992] for porous media or *Longino and Kueper* [1999] for fractures.

While the geometric characteristics of the individual blobs is independent of the “path” taken during mobilization, i.e., water versus surfactant flood, the average saturation after mobilization will be path-dependent because of the very different mechanisms that act during the mobilization process. In water

floods, rivulet formation tends to leave a more sparsely filled blob field, while the mobilization front that forms during surfactant floods will sweep the entire domain width and leave NAPL behind in every pore that is not excluded by viscous forces. This observation is supported by the results shown in Figure 8, where the number of entrapped blobs after surfactant floods is higher than that after water floods at similar  $N_{ca}$  (Figure 8c versus Figure 8d and Figure 8f versus Figure 8g). In Figure 10 the number of entrapped blobs within the micro-model is plotted as a function of  $N_{ca}$ . The results in Figure 10 indicate that for a similar  $N_{ca}$  a significantly higher number of blobs is obtained in surfactant floods than that in water floods, when  $N_{ca} < 10^{-3}$ .

The differences in blob numbers between water and surfactant floods translate directly into differences in average saturation. As shown in Figure 11, a significantly higher residual

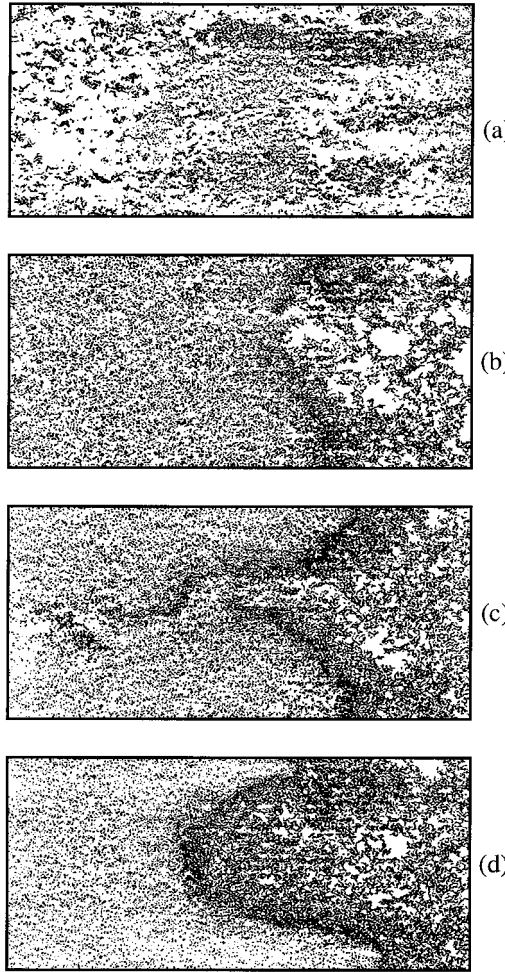


**Figure 6.** Images of the mobilization front: (a) experiment 11, 0.51 PV of water flood, IFT = 34.5 dyn/cm,  $v = 2.75$  cm/s, and  $N_{ca} = 1.0 \times 10^{-3}$ ; (b) experiment 1, 0.47 PV of surfactant flood, IFT = 0.98 dyn/cm,  $v = 0.020$  cm/s, and  $N_{ca} = 2.9 \times 10^{-4}$ ; (c) experiment 3, 0.52 PV of surfactant flood, IFT = 0.68 dyn/cm,  $v = 0.020$  cm/s, and  $N_{ca} = 4.2 \times 10^{-4}$ ; and (d) experiment 5, 0.39 PV of surfactant flood, IFT = 0.23 dyn/cm,  $v = 0.02$  cm/s, and  $N_{ca} = 1.2 \times 10^{-3}$ . Direction of flow is from left to right in images. Black pixels indicate areas where NAPL is present. White pixels indicate areas where aqueous phase is present.

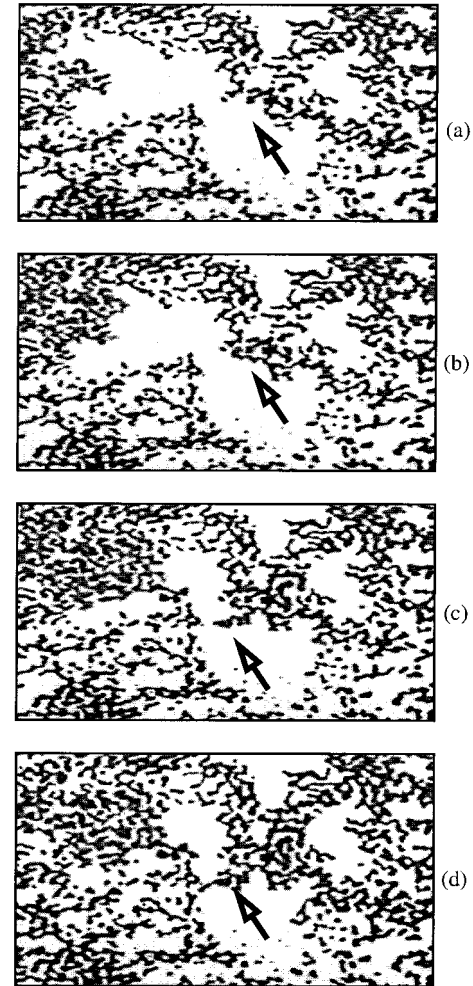


**Figure 7.** Series of images demonstrating the migration of NAPL blobs (right to left) against the average direction of flow (left to right) in experiment 8. Arrows point to the location of the upstream migration. Images in Figures 7a–7d were captured at 15 s time intervals. The area of the micromodel in the image is 6.5 cm by 4.5 cm. Direction of flow is from left to right in images. Black to gray pixels indicate areas where NAPL is present. White pixels indicate areas where aqueous phase is present.

saturation is obtained with surfactant floods for a given  $N_{ca}$ , when  $N_{ca} < 10^{-3}$ . According to current conceptual models [e.g., Lake, 1989] the residual NAPL saturation following mobilization should scale to the capillary number, for a given pore structure. That is, the same residual saturation should be reached for a specified  $N_{ca}$ . However, we find clear differences in residual TCE saturation due to the different underlying mechanisms of front versus rivulet formation and, thus, a “path” dependence. We note that this discrepancy between water and surfactant floods is far beyond what can be attributed to our error in determining  $N_{ca}$  or the saturations. Furthermore, if our implicit assumption that the contact angles are zero for both the water and surfactant floods is incorrect, this error would not explain the magnitude of the difference between the water and surfactant desaturation results. The general trends in the capillary desaturation curves shown in Figure 11 are similar to those found in the literature [e.g., Lake, 1989], where the majority of the nonwetting phase is displaced for

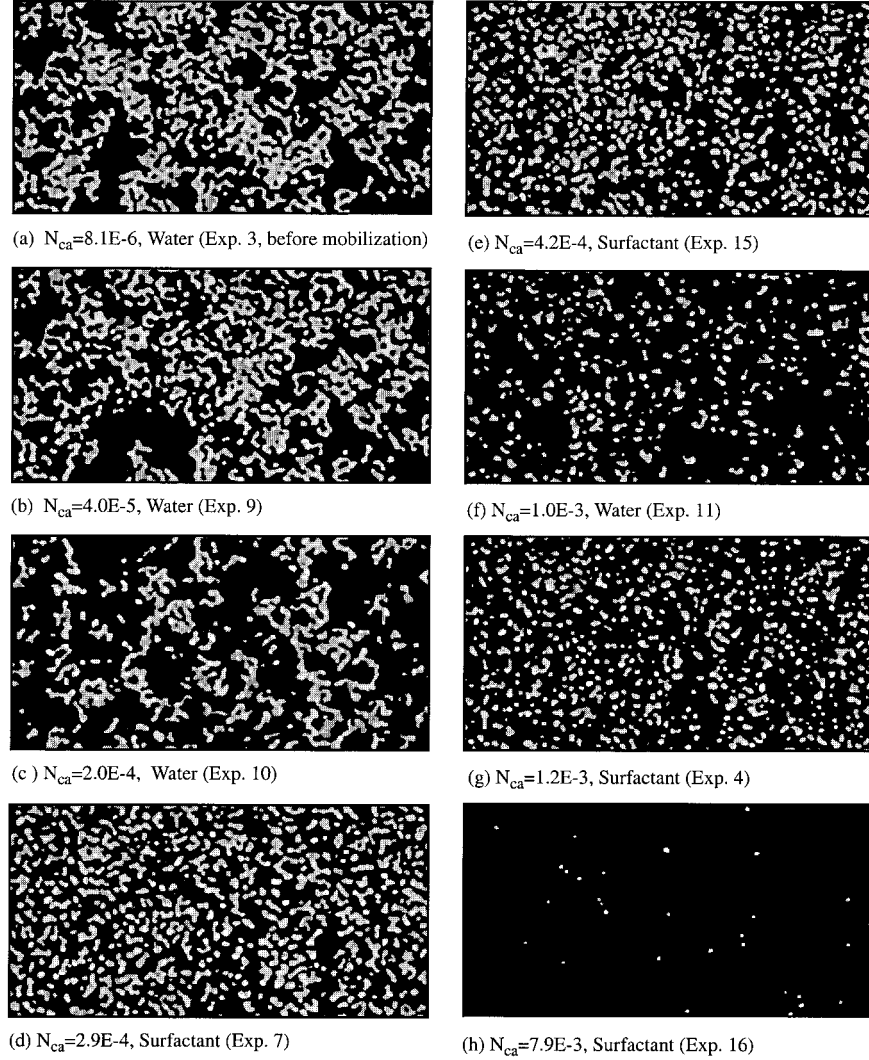


**Figure 8.** Images of NAPL blobs following mobilization as a function of capillary number and flood type. Images in Figures 8a–8h show the same region in the micromodel and have a size of 250 by 400 pixels (3.8 cm by 6.1 cm). NAPL and aqueous phase are white and black, respectively. Direction of flow is from left to right in images. Figure 8a is an image taken after the water flood stage and before the mobilization stage for experiment 3. Black pixels indicate areas where only aqueous phase is present. Gray pixels indicate areas where NAPL is present. Read 8.1E-6 as  $8.1 \times 10^{-6}$ .

$N_{ca} > 10^{-3}$ , and complete displacement occurs at about  $N_{ca} = 10^{-2}$ . *Mahers et al.* [1981] present capillary desaturation curves for high- and low-IFT mobilization floods. The results of *Mahers et al.* [1981] do not indicate any significant difference in trends of saturation versus  $N_{ca}$  between the high- and low-tension floods; however, their experiments were conducted over a more narrow range of  $N_{ca}$  than the results given here.

### 3.3. Solubilization of Residual NAPL

Shown in Figure 12 are images of the solubilization flood at increasing pore volumes from experiments 1, 6, 10, and 11. The formation and propagation of dissolution fingers (clear areas) can be observed in these images. Dissolution fingering has been explained as a result of instabilities that develop at the solubilization front [Imhoff *et al.*, 1996]. As the fingers propagate through the field, three fingers typically grow faster than the others, become dominant, and eventually break through

the effluent end of the micromodel. The locations of the three dominant fingers correspond to the preferential flow zones where the velocity was shown to be higher in the dye transport experiment (Figure 3). The influence of solubilization capacity of surfactant solutions and initial NAPL saturations also is demonstrated in Figure 12. When the initial NAPL saturation is the same, the dissolution fingers develop and propagate faster when the solubility is higher (experiment 6 versus experiment 1). When the solubility is held constant, the fingers grow and propagate faster when the initial NAPL saturation is lower (experiment 6 versus experiment 10 versus experiment 11). These results, demonstrating the influence of the permeability field, solubility, and NAPL saturation are all in agreement with the observations of *Imhoff et al.* [1996] in pure water/NAPL systems.

Plotted in Figure 13 are the mass removal rates, normalized by the solubilization rate that would occur under equilibrium conditions (defined as volumetric flow rate multiplied by the

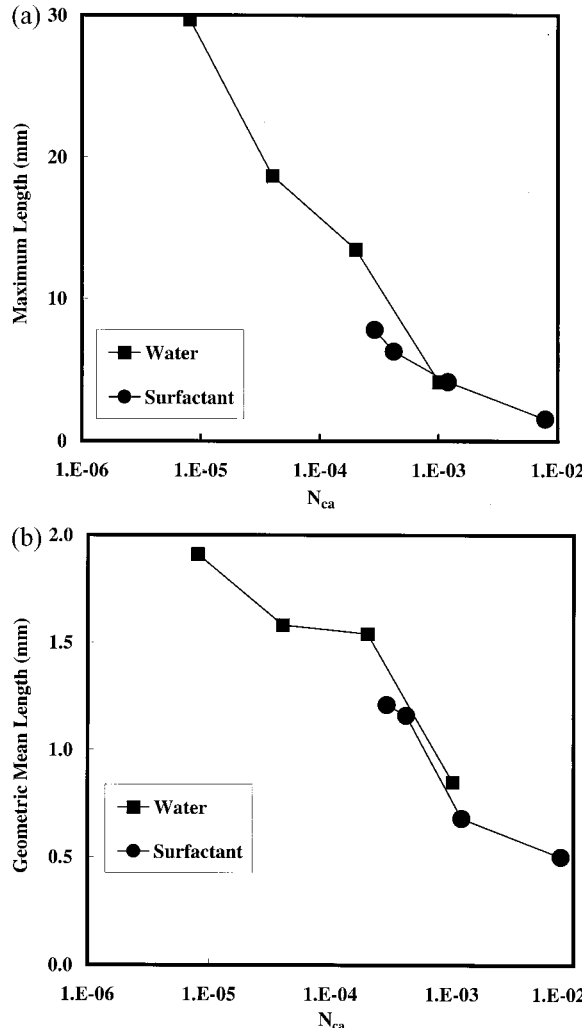


**Figure 9.** (a) Maximum and (b) geometric mean blob lengths in the average direction of flow versus capillary number following mobilization.

solubility concentration corresponding to the surfactant composition), for the same experiments as shown in Figure 12. The number of pore volumes associated with dissolution finger breakthrough at the end of the micromodel is depicted in

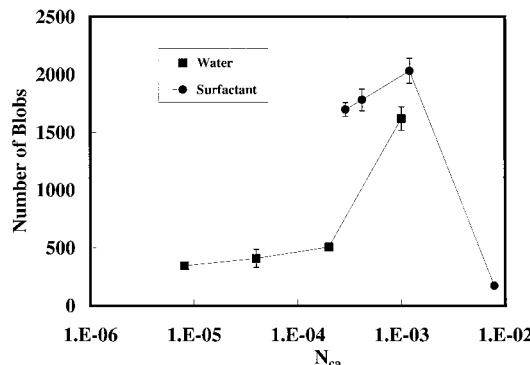


**Figure 10.** Number of blobs versus capillary number following mobilization. Each symbol represents averages over replicate experiments. Error bars indicate 1 standard deviation from the mean, where replicate experiments were conducted.

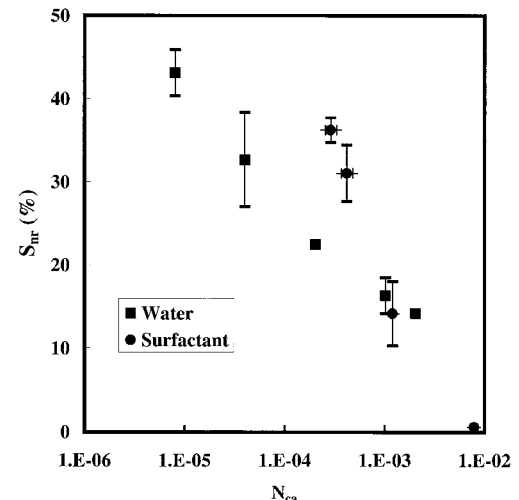


**Figure 11.** Capillary desaturation for water mobilization and surfactant mobilization floods. Symbols represent averages over replicate experiments. Error bars in the  $y$  axis direction represent 1 standard deviation for residual NAPL saturations from the replicate experiments. Error bars in the  $x$  axis direction represent the uncertainty in the capillary number associated with the IFT measurements (1 standard deviation).

Figure 13 for each experiment. During the early stages of the solubilization experiments the NAPL removal rates are higher than the equilibrium rate in three of the four experiments, indicating that some NAPL mobilization was occurring. After the early stage and before finger breakthrough the NAPL removal rates are at or close to the equilibrium solubilization rate. After finger breakthrough the normalized mass removal rates decrease considerably. Figure 14 shows the effluent TCE concentration measured in aqueous samples normalized by the equilibrium concentration for experiment 14. The normalized effluent TCE concentration assuming equilibrium conditions is given in Figure 14 for comparison purposes. Images of the fingers at the outflow edge of the micromodel for the associated pore volumes flushed are also shown. Equilibrium concentrations were reached between one and two pore volumes (PV) and remain relatively constant until  $\sim 20$  PV. Effluent concentrations are again seen to decrease with the breakthrough of dissolution fingers.

These results illustrate that for the flow velocities and NAPL-surfactant system used in this study, observations of macroscale nonequilibrium will be dominated by dissolution fingering, with a chemical rate limitation or a mass transfer resistance playing a less significant role, if any. The dissolution fingering produces the observed nonequilibrium behavior because the portion of the aqueous phase flowing through the clear fingers (where the NAPL has been eliminated) has dissolved NAPL concentrations significantly below equilibrium (solubility) levels. The remaining portion of the aqueous phase flow occurs in areas containing residual NAPL, where one would expect the dissolved NAPL concentrations to be near or at equilibrium, given sufficient residence time. Thus the width-averaged dissolved NAPL concentration yields an observed nonequilibrium behavior.

During several of the solubilization experiments the spontaneous formation of a translucent or gray phase was observed in the micromodel. Figure 15 shows the occurrence of the gray phase (dark gray areas) in experiment 1, along with aqueous

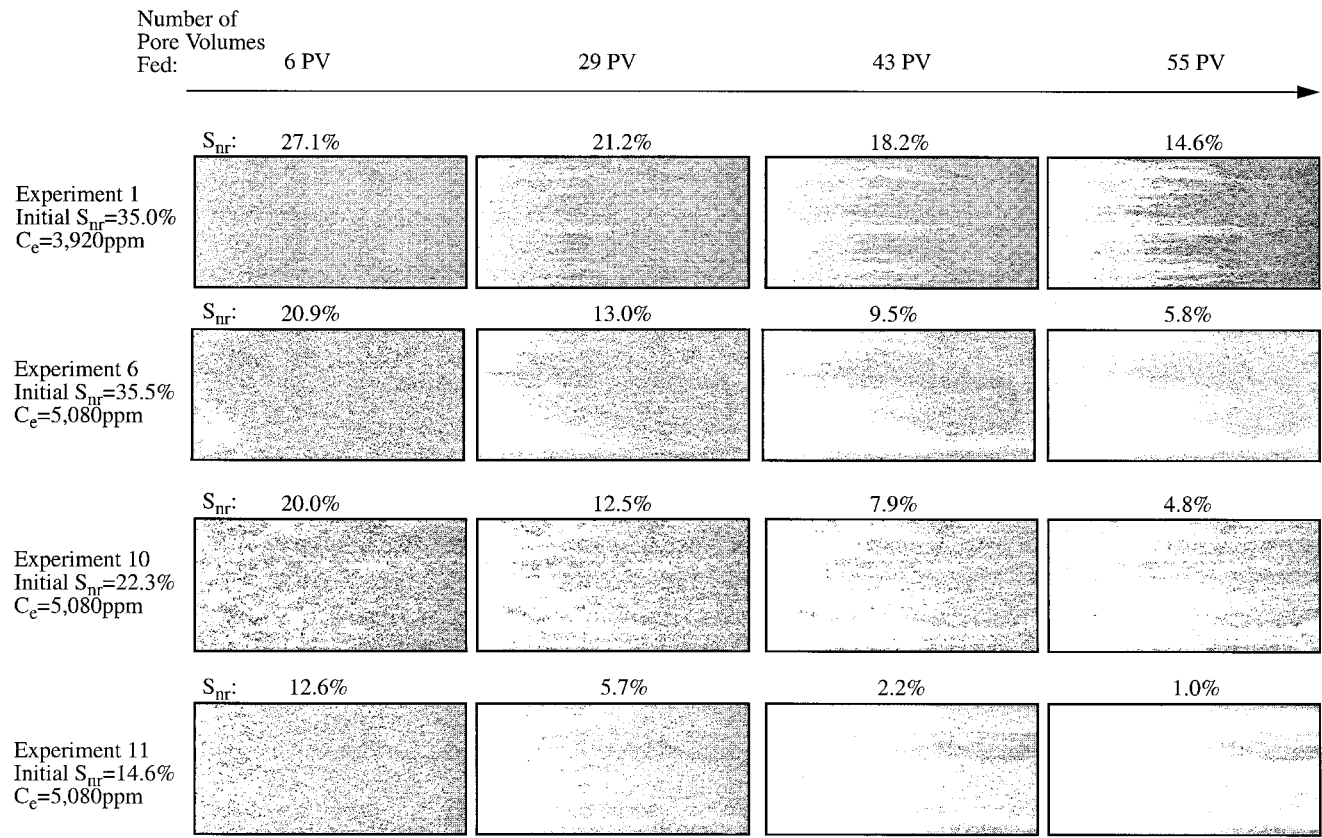


**Figure 12.** Influence of solubility and initial NAPL saturation on solubilization and formation of dissolution fingers. The NAPL saturation corresponding to each image is given at the top of the image. The axis at the top of the figure indicates the number of pore volumes fed corresponding to the images below the axis. Direction of flow is from left to right in the images. Black to gray pixels indicate areas where NAPL or macroemulsion is present. White pixels indicate areas where aqueous surfactant solution is present.  $S_{nr}$ , residual NAPL saturation;  $C_e$ , equilibrium, or solubility, concentration.

phase (white to light gray areas) and residual NAPL (black blobs). The gray phase is most likely a macroemulsion, consisting of small, light-scattering droplets of NAPL surrounded by surfactant molecules suspended in the aqueous phase. Mac-

roemulsions usually are considered to be unstable, meaning that the NAPL droplets should eventually coalesce. However, once the macroemulsion formed in the micromodel, it persisted, indicating that the time required for coalescence of the NAPL droplets in this system is longer than the residence time of the macroemulsion in the micromodel.

The macroemulsion appeared in areas where the local NAPL saturation was relatively high, as indicated by the absence of the macroemulsion in the upgradient portion of the micromodel in Figure 15, where the majority of the NAPL has been solubilized. In addition, the macroemulsion was not observed inside the dissolution fingers, as is also shown in Figure 15. This observation implies that the formation and persistence of the macroemulsion depends on saturation, a dependency that also was reported by Okuda *et al.* [1996] in batch NAPL-surfactant experiments. In the case of the micromodel solubilization experiments the local saturation dependency is related to the availability of NAPL to sustain the high dissolved concentration required to form suspended macroemulsions in the aqueous phase.

Occurrence of the macroemulsion also is correlated with the surfactant formulation. As the salt concentration increased, the formation and persistence of the macroemulsion decreased. This result could be explained by either of two factors. First, the spontaneous formation of the macroemulsion may be prevented, or at least minimized, at high salt concentrations

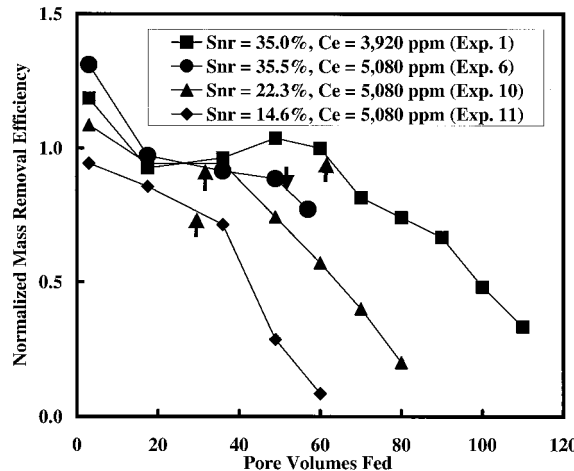


**Figure 13.** NAPL mass removal rate normalized by the rate that would occur during equilibrium conditions versus number of pore volumes fed as a function of starting NAPL saturation. Arrows indicate the number of pore volumes fed corresponding to finger breakthrough for each experiment.

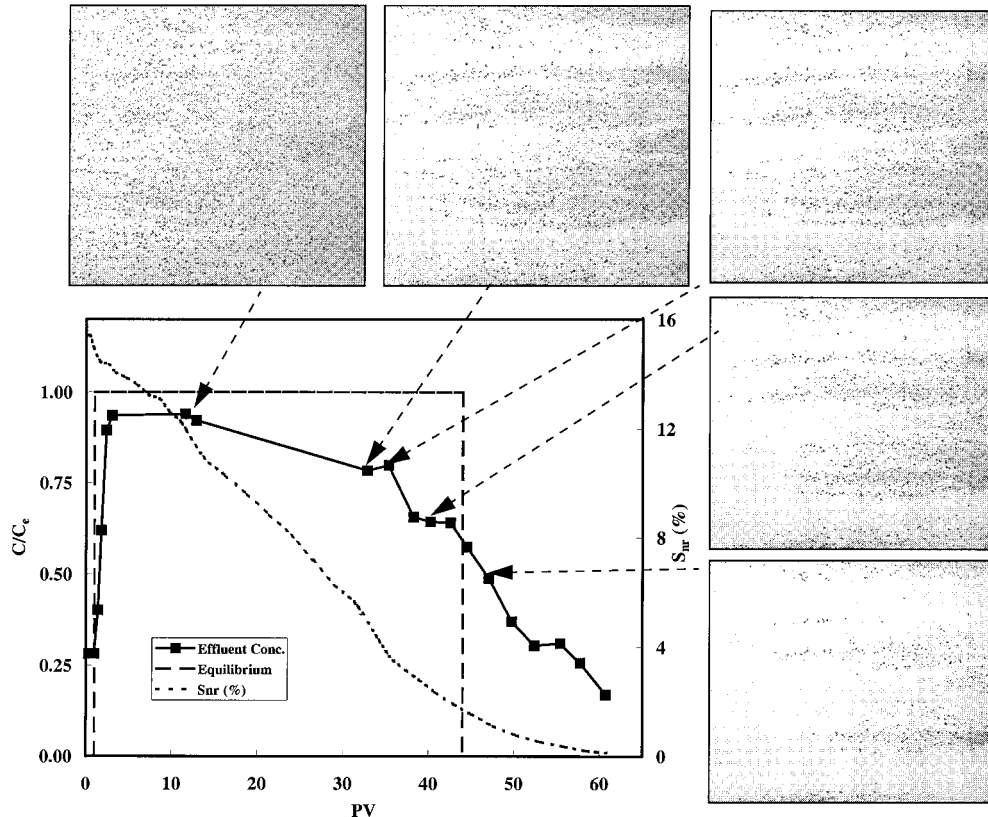


**Figure 14.** Normalized effluent TCE concentration (solid line and symbols) and residual saturation (short-dashed line) versus number of pore volumes fed for experiment 12. The long-dashed line represents the effluent concentration expected if equilibrium conditions were occurring. Attached are images (15 cm by 13.5 cm) of the outflow edge of the micromodel for the corresponding number of pore volumes. Direction of flow is from left to right in images. Black to gray pixels indicate areas where NAPL or macroemulsion is present. White to lighter gray pixels indicate areas where aqueous surfactant solution is present.

because of the change in electrolyte chemistry in the aqueous solution. Second, higher salt concentrations result in reduced interfacial tensions and consequently lower residual saturations following the mobilization stage. Thus the reduced occurrence of the macroemulsion at higher salt concentrations could simply be due to the coincidentally reduced NAPL saturations within the micromodel.

Macroemulsion formation and persistence could have a sig-

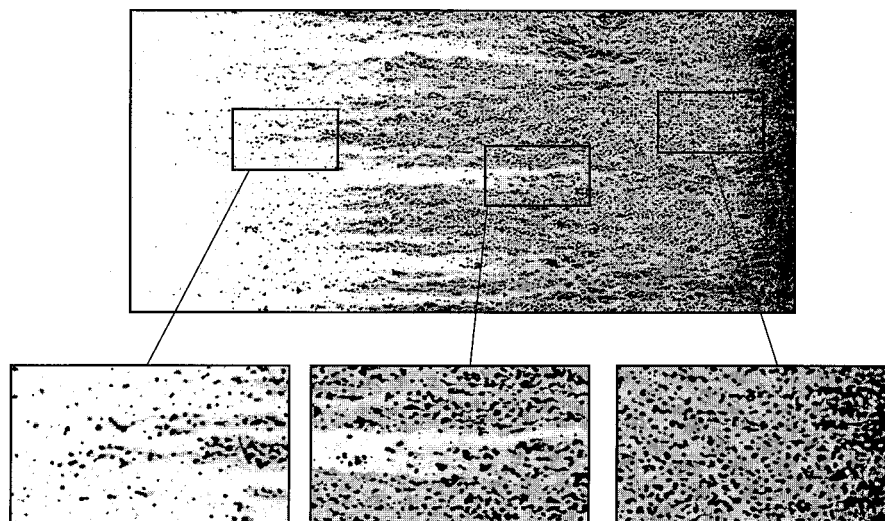


**Figure 15.** Macroemulsion occurrence during solubilization in experiment 1. The white areas in the images are regions of aqueous surfactant solution, the black areas are NAPL blobs, and the gray areas are aqueous surfactant solution with macroemulsion. Direction of flow is from left to right in images.

nificant impact on solubilization rates because a mobile macroemulsion phase would be capable of transporting apparent concentrations of NAPLs that are considerably higher than the solubility limit. We did not observe concentrations significantly higher than the solubility limit in the micromodel effluent when macroemulsion was present; however, effluent concentrations were measured in only two of the experiments where macroemulsions were observed. Macroemulsions also can have the effect of increasing the mobile fluid viscosity, which would in turn reduce the aqueous phase permeability [Okuda *et al.*, 1996]. We did not measure the viscosity of the macroemulsion phase directly; however, we did not observe any significant variations in aqueous phase flow patterns when the macroemulsion was present, as compared to cases where the macroemulsion occurrence was reduced or absent.

#### 4. Conclusions

A micromodel and quantitative visualization system were applied to observe surfactant-enhanced NAPL mobilization and solubilization phenomena at the microscale. The micromodel consisted of two plates of textured glass held in contact, producing a series of variably sized, connected apertures available for fluid flow. The quantitative visualization system was capable of resolving micromodel aperture geometry and the evolution of NAPL phase structure and saturation. For each experiment a common residual NAPL field was established with a NAPL flood into the water-saturated micromodel followed by a water flood at low flow rates. We then conducted a series of mobilization-solubilization experiments where the chemical formulation of the flood was varied from pure water to floods containing an anionic surfactant and cosolvent at fixed concentrations and a range of electrolyte concentrations. The variations in the electrolyte concentrations provided a range of IFTs and NAPL solubilities. For the surfactant floods the flow rate was kept at the same rate used to establish the residual NAPL, yielding a final  $N_{ca}$  modified only by changes in the IFT. For the pure water floods the flow rate was varied to modify the  $N_{ca}$  by changes in viscous forces alone. Following the pure water floods, subsequent solubilization with a fixed surfactant chemistry allowed the investigation of initial NAPL saturation on the surfactant-enhanced solubilization process.

For a given  $N_{ca}$  we found significant differences in the macroscale saturation at the end of the mobilization stage of the experiments, for  $N_{ca} < 10^{-3}$ . The observed differences occur because the changes in the local  $N_{ca}$  during the surfactant floods take place through a miscible displacement process, while during pure water floods, changes in the local  $N_{ca}$  are established immediately throughout the field. This path dependency, i.e., changes in the local  $N_{ca}$  via increases in viscous forces or via miscible IFT reduction, is in turn caused by differences in microscale processes. For the surfactant floods a high NAPL saturation front forms normal to the direction of flow and sweeps the entire field width. The IFT reduction fronts form because of the combination of  $N_{ca}$ -induced downstream and capillary-driven upstream mobilization processes. For the water floods, rivulets oriented in the direction of flow form and are driven downstream. Rivulet formation occurs through the simultaneous application of viscous forces in primarily a single direction throughout the field. These very different, path-dependent, microscale processes between the surfactant and pure water floods lead to a difference in final

macroscale saturation. The differences in saturation are attributed to differences in the number of remaining, entrapped NAPL blobs, rather than differences in final blob size statistics.

Solubilization of the residual NAPL remaining after the mobilization stage was dominated by the formation of dissolution fingers. The fingers developed and propagated faster at lower residual NAPL saturations and when the aqueous phase solubility was higher. The location of finger initiation and propagation was directly related to spatial heterogeneity in the aperture field. Equilibrium NAPL mass removal rates were observed before the dissolution fingers broke through the effluent edge of the micromodel. Following finger breakthrough, the solubilization rate decreased below the rate expected if equilibrium solubilization were occurring throughout the micromodel and continued to decline as the back of the dissolution finger zone advanced to the downstream boundary. Thus, at the flow rates and chemical formulations considered in our experiments, macroscale nonequilibrium NAPL solubilization can be attributed directly to the development of a dissolution finger zone where significant heterogeneity occurs because of microscale dissolution fingering.

A macroemulsion phase was observed to form spontaneously and persist during portions of the solubilization stage of the experiments. The occurrence of the macroemulsion was related directly to local NAPL saturation, where macroemulsion formation was found to be more likely at higher local NAPL saturations and was at least indirectly related to electrolyte concentration in the surfactant formulation. The impact of macroemulsion on solubilization rates is unclear, since micromodel effluent concentrations and aqueous phase flow patterns did not appear to be affected by macroemulsion occurrence.

**Acknowledgments.** This work has been funded by the U.S. Environmental Protection Agency ORD/NCERQA at Michigan Technological University (grant agreement R824505-01-0) and the U.S. Department of Energy's Basic Energy Science Geoscience Program and Environmental Management Science Program at Sandia National Laboratories (contract DE-AC04-94AL85000). Experiments were conducted in the Flow Visualization and Processes Laboratory at Sandia National Laboratories. We thank William J. Peplinski and Donald Fox for assistance in modifying and setting up the experimental system and data processing procedures.

#### References

- Conrad, S. H., J. L. Wilson, W. R. Mason, and W. J. Peplinski, Visualization of residual organic liquid trapped in aquifers, *Water Resour. Res.*, 28(2), 467–478, 1992.
- Detwiler, R. L., S. E. Pringle, and R. J. Glass, Measurement of fracture aperture fields using transmitted light: An evaluation of measurement errors and their influence on simulations of flow and transport through a single fracture, *Water Resour. Res.*, 35(9), 2605–2617, 1999.
- Detwiler, R. L., H. Rajaram, and R. J. Glass, Solute transport in variable-aperture fractures: An investigation of the relative importance of Taylor dispersion and macropdispersion, *Water Resour. Res.*, 36(7), 1611–1626, 2000.
- Deutsch, C. V., and A. G. Journel, *GSLIB: Geostatistical Software Library and User's Guide*, 2nd ed., Oxford Univ. Press, New York, 1998.
- Egbogah, E. O., and R. A. Dawe, Microvisual studies of size distribution of oil drops in porous media, *Bull. Can. Pet. Geol.*, 28, 200–210, 1980.
- Glass, R. J., and M. J. Nicholl, Quantitative visualization of entrapped phase dissolution within a horizontal flowing fracture, *Geophys. Res. Lett.*, 22(11), 1413–1416, 1995.
- Glass, R. J., and M. J. Nicholl, Physics of gravity driven fingering of immiscible fluids within porous media: An overview of current un-

- derstanding and selected complicating factors, *Geoderma*, 70, 133–163, 1996.
- Glass, R. J., S. H. Conrad, and W. Peplinski, Gravity-destabilized nonwetting phase invasion in macroheterogeneous porous media: Experimental observations of invasion dynamics and scale analysis, *Water Resour. Res.*, 36(11), 3121–3137, 2000.
- Hornbrook, J. W., L. M. Castanier, and P. A. Pettit, Observation of foam oil interactions in a new high-resolution micromodel, paper presented at 66th Annual Technical Conference and Exhibition of SPE, Soc. of Pet. Eng., Dallas, Tex., 1991.
- Imhoff, P. T., G. P. Thyrum, and C. Miller, Dissolution fingering during the dissolution of nonaqueous phase liquids in saturated media, 2, Experimental observations, *Water Resour. Res.*, 32(7), 1929–1942, 1996.
- Jia, C., K. Shing, and Y. C. Yortsos, Visualization and simulation of non-aqueous phase liquids solubilization in pore networks, *J. Contam. Hydrol.*, 25, 363–387, 1999.
- Lake, L., *Enhanced Oil Recovery*, Prentice Hall, Englewood Cliffs, N. J., 1989.
- Larson, R. G., The influence of phase behavior on surfactant flooding, *Soc. Pet. Eng. J.*, 31, 411–422, 1979.
- Larson, R. G., and G. J. Hirasaki, Analysis of the physical mechanisms in surfactant flooding, *Soc. Pet. Eng. J.*, 30, 42–58, 1978.
- Longino, B. L., and B. H. Kueper, Nonwetting phase retention and mobilization in rock fractures, *Water Resour. Res.*, 35(7), 2085–2093, 1999.
- Mahers, E. G., R. J. Wright, and R. A. Dawe, Visualization of the behavior of EOR reagents in displacements in porous media, in *Enhanced Oil Recovery, Proceedings of the Third European Symposium on Enhanced Oil Recovery*, edited by F. J. Fayer, Elsevier Sci., New York, 1981.
- Mayer, A. S., and C. T. Miller, The influence of porous media characteristics and measurement scale on pore-scale distributions of residual nonaqueous phase liquids, *J. Contam. Hydrol.*, 11, 189–213, 1992.
- Mayer, A. S., and C. T. Miller, An experimental investigation of pore-scale distribution of nonaqueous phase liquids at residual saturation, *Transp. Porous Media*, 10, 1057–1085, 1993.
- Mayer, A. S., L. Zhong, and G. A. Pope, Measurement of mass transfer rate for surfactant-enhanced solubilization of nonaqueous phase liquids, *Environ. Sci. Technol.*, 33, 2965–2972, 1999.
- Mercer, J. W., and R. M. Cohen, A review of immiscible fluid in the subsurface: Properties, models, characterization and remediation, *J. Contam. Hydrol.*, 6, 107–163, 1990.
- Nicholl, M. J., and R. J. Glass, Wetting phase permeability in a partially saturated horizontal fracture, paper presented at 5th Annual International High Level Radioactive Waste Management Conference, Am. Nucl. Soc., Las Vegas, Nev., 1994.
- Nicholl, M. J., R. J. Glass, and H. A. Nguyen, Small-scale behavior of single gravity driven fingers in an initially dry fracture, paper presented at 4th International Conference of High Level Radioactive Waste Management, Am. Nucl. Soc., Las Vegas, Nev., April 26–30, 1993.
- Nicholl, M. J., H. Rajaram, R. J. Glass, and R. Detwiler, Saturated flow in a single fracture: Evaluation of the Reynolds equation in measured aperture fields, *Water Resour. Res.*, 35(11), 3361–3373, 1999.
- Okuda, I., J. F. McBride, S. N. Gleyzer, and C. T. Miller, Physicochemical transport process affecting the removal of residual NAPL by nonionic surfactant solutions, *Environ. Sci. Technol.*, 30, 1852–1860, 1996.
- Pope, G. A., The application of fractional flow theory to enhanced oil recovery, *SPEJ Soc. Pet. Eng. J.*, 32, 191–205, 1980.
- Tidwell, V. C., and R. J. Glass, X ray and visible light transmission for laboratory measurement of two-dimensional saturation fields in thin-slab systems, *Water Resour. Res.*, 30(11), 2873–2882, 1994.
- Wardlaw, N. C., and M. McKellar, Oil blob populations and mobilization of trapped oil in unconsolidated packs, *Can. J. Chem. Eng.*, 63, 525–532, 1985.
- 
- R. J. Glass, Flow Visualization and Processes Laboratory, Sandia National Laboratories, Mail Stop 735, Albuquerque, NM 87185-0735. (rjglass@sandia.gov)
- A. Mayer, c/o M. Hassanzadeh, Department of Hydrology and Ecology, Faculty of Civil Engineering and Geosciences, Delft University of Technology, P.O. Box 5048, 2600 HA Delft, Netherlands. (asmayer@mtu.edu)
- L. Zhong, Center for Petroleum and Geosystems Engineering, University of Texas, Austin, TX 78712.

(Received October 14, 1999; revised July 26, 2000; accepted September 21, 2000.)

